Published in final edited form as:

Sci Total Environ. 2021 January 01; 750: 141202. doi:10.1016/j.scitotenv.2020.141202.

Alteration of yellow traffic paint in simulated environmental and biological fluids

Michael J. O'Shea[a,*], **Ruggero Vigliaturo**[a], **Jessica K. Choi**[a], **Thomas P. McKeon**[b], **Mark P.S. Krekeler**[c,d], **Reto Gieré**[a,b]

[a]Department of Earth and Environmental Science, University of Pennsylvania, Philadelphia, PA 19104-6316, USA

[b]Center of Excellence in Environmental Toxicology, University of Pennsylvania, Philadelphia, PA 19104-6316, USA

[c]Department of Geology and Environmental Earth Science, Miami University Hamilton, Hamilton, OH 45011, USA

[d]Department of Geology and Environmental Earth Science, Miami University, Oxford, OH 45056, USA

Abstract

Pollution from heavy metals in urban environments is a topic of growing concern because many metals, including Pb and Cr, are a human health hazard. Exposure to Pb and Cr has been linked to the inhibition of neurological development as well as toxic effects on many organs. Yellow traffic paint (YTP) is a mixture that contains organic polymers, binders, and pigments, which in some cases consist of crocoite ($PbCrO_4$) that may be coated by silica. The primary aim of this study was to investigate the behavior of the crocoite pigment grains within YTP and their silica coatings in simulated environmental and human body conditions. To do this, both YTP and asphalt were collected in Philadelphia, PA, USA. These samples as well as a standard $PbCrO_4$ were investigated with powder X-ray diffraction, X-ray fluorescence, environmental scanning electron microscopy (ESEM), transmission electron microscopy, and energy-dispersive X-ray spectroscopy. Using this multi-analytical approach, mineral phases were determined in the YTP, their shape, dimensional distributions, crystallinity, and chemical composition, as well as elemental distributions before and after experimental interactions. Three batch dissolution experiments with YTP, asphalt, and standard $PbCrO_4$were performed to simulate ingestion, inhalation, and environmental interaction with rainwater. Elemental releases were determined with inductively coupled plasma-optical

*Corresponding author. michajo@sas.upenn.edu (M.J. O'Shea).

CRediT authorship contribution statement

Michael J. O'Shea: Conceptualization, Methodology, Investigation, Writing - original draft, Writing - review & editing, Visualization. **Ruggero Vigliaturo:** Conceptualization, Methodology, Investigation, Writing - review & editing, Visualization. **Jessica K. Choi:** Methodology, Investigation, Writing - review & editing. **Thomas P. McKeon:** Data curation, Writing - review & editing. **Mark P.S. Krekeler:** Supervision, Writing - review & editing. **Reto Gieré:** Conceptualization, Writing - review & editing, Supervision, Funding acquisition.

Declaration of competing interest

The authors have no conflicts of interests to declare.

Appendix A. Supplementary data

Supplementary data to this article can be found online at https://doi.org/10.1016/j.scitotenv.2020.141202.

emission spectrometry, and results indicated that little (ingestion) to no (environmental and inhalation) Pb and Cr were leached from the YTP during the three experimental procedures. This is likely due to the silica coating that encapsulates the crocoite particles, which persisted during all interactions. The ESEM results for YTP showed dimensional reductions after interactions with all three fluids. The silica coating must be further explored to determine how it breaks down in real environmental conditions.

Graphical Abstract

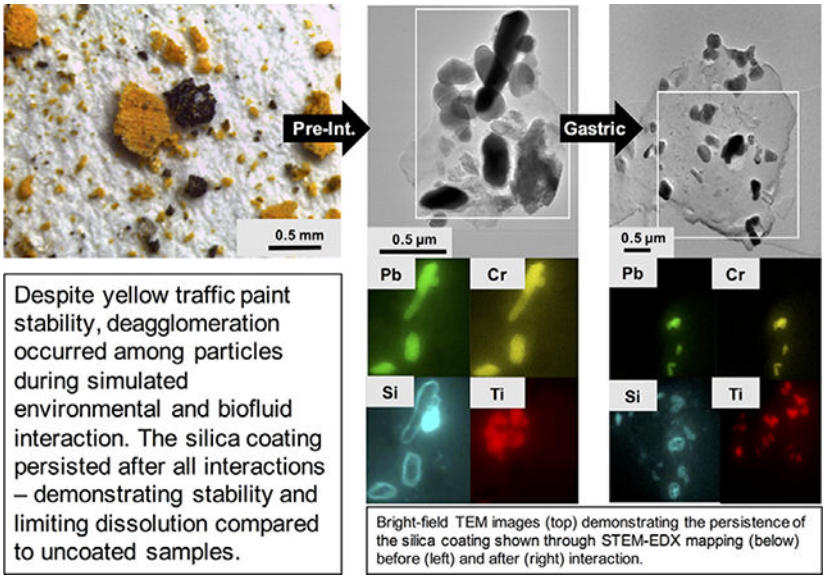

Keywords

Crocoite; Chemical evolution; Simulated biofluids; Yellow traffic paint; Silica coating; Electron microscopy

1. Introduction

Metal contamination is a significant concern in the urban environment (Romieu et al., 1994; Chon et al., 1995; Li et al., 2001; Charlesworth et al., 2011; Bavec et al., 2014; Padoan et al., 2017; Dietrich et al., 2018; Gaberšek and Gosar, 2018; Dietrich et al., 2019), and the impact of environmental contamination is expected to increase with growing urban populations (United Nations, 2014). Two key metals of environmental and human health concern are Pb and Cr. The most common anthropogenic sources of Pb are emissions from oil, coal, and leaded gasoline combustion, Pb-based pesticides, waste incineration, smelters, solders, and paints (e.g., Agency for Toxic Substances and Disease Registry [ATSDR], 2019). Urban road dust and soils are commonly studied to gauge the level of Pb pollution as they act as both source and sink for contamination (e.g., Laidlaw and Filippelli, 2008; Duong and Lee, 2011; Laidlaw and Taylor, 2011; LeGalley et al., 2013; Lusby et al., 2015; Padoan et al., 2017; O'Shea et al., 2020). Exposure to Pb commonly occurs from the inhalation of dusts and the ingestion of contaminated soils, paint chips, and drinking water (e.g., Alatise and

Schrauzer, 2010; Yoshinaga et al., 2014; Bi et al., 2015; Walraven et al., 2015; Council on Environmental Health, 2016). Lead is acutely toxic to most human organs, has detrimental impacts on childrens' cognitive development, and, along with Cr, is on the ATSDR/ Environmental Protection Agency's (EPA) Substance Priority List (e.g., Anttila et al., 1995; Alatise and Schrauzer, 2010; Council on Environmental Health, 2016; ATSDR, 2017). Both Pb(II) and Pb(VI) may be found in the environment (e.g., Reeder and Schoonen, 2006). Chromium is thought to be ubiquitous in the urban environment and can be found in various alloys, electroplating, wood preservatives, leather tanning, anticorrosive agents, and paints. One common pathway for Cr exposure is through inhalation in industrial settings (Leonard et al., 2004). Other routes of Cr exposure include the ingestion of contaminated drinking water or soils (e.g., ATSDR, 2012). Chromium's valence state in minerals varies from Cr(II) to Cr(VI) and, depending on the valence state, Cr can be a micronutrient (Anderson, 1998) or a human health hazard (e.g., Lee et al., 2018). Chromium(VI) is a carcinogen that has no minimum threshold to trigger a carcinogenic response (Alexeeff et al., 1989; Collins et al., 2010; Haney et al., 2014). Over the past few decades, some countries have introduced more stringent regulations on the use of Pb and Cr; these regulations were informed by studies that have characterized the extent of Pb and Cr pollution in the environment and/or outlined the associated health risks (e.g., International Agency for Research on Cancer, 2006; Wadanambi et al., 2008; Holecy and Mousavi, 2012; Datko-Williams et al., 2014; Gottesfeld et al., 2014; Gottesfeld, 2015; Turner and Lewis, 2018; United Nations and World Health Organization, 2019).

Despite multiple studies identifying Pb-bearing paint as a source of contamination, including in road dusts and soils, Pb and Cr(VI) are still commonly used in yellow traffic paints (YTP) including in the US (e.g., Romieu et al., 1994; Lanphear et al., 1998; Adachi and Tainosho, 2004; Murakami et al., 2007; Turner and Solman, 2016). Pigments containing crocoite ($PbCrO_4$) are often used to provide a yellow color and are mixed with organic polymers and binders to form paint (Jeffs and Jones, 1999; Walraven et al., 2015). A number of studies have found that $PbCrO_4$ may be carcinogenic, cytotoxic, and genotoxic (e.g., Sidhu et al., 1991; Xu et al., 1992; Singh et al., 1999). However, these pigments are in many cases coated by silica that inhibits or delays $PbCrO_4$ dissolution, thus lowering the bioavailability of Pb and Cr and reducing potential danger to human health (Pier et al., 1991). Additionally, $PbCrO_4$ pigments are often coated with silica to increase their resistance to abrasion (Linton, 1972). A recent study demonstrated, however, that the silica coating of $PbCrO_4$ pigments can be degraded in environmental conditions (Lee et al., 2018). This silica coating must therefore be experimentally tested to establish how it may break down.

Similarly, YTP should be investigated as it likely contributes to Pb and Cr pollution (White et al., 2014; Lee et al., 2016; Turner et al., 2016; Turner and Solman, 2016; Meza-Figueroa et al., 2018). Ingestion must be considered as it is the primary pathway by which people may interact with YTP particles; inhalation must also be explored as $PbCrO_4$ from YTP has been found in black carbon particles, which have been airborne (Lee et al., 2018). In this study, we aim to improve our understanding of these poorly known aspects of YTP. To achieve these goals, we designed experiments that simulate environmental and human body interactions with YTP and characterized the chemical and morphologic evolution of YTP. We discuss the persistence of crocoite's silica coating and its properties at the nanoscale.

Our study enhances the knowledge on the behavior of YTP and on how the silica coatings of crocoite may inhibit its dissolution in environmental and human body interactions.

2. Methods

2.1. Sampling, sample preparation, and geographic information systems (GIS)

Three samples of YTP were collected along 41st Street at three separate points between Pine and Spruce streets in Philadelphia, PA using methods similar to those applied in a comparable study (White et al., 2014). These samples were taken from double yellow lines by gentle brushing and scraping, thus removing loose paint chips. The three individual samples were then combined into one composite sample, which was used for all experiments. Asphalt was sampled at the same locations to provide a control material representative of the road surface. All samples were immediately placed in polyethylene plastic bags and stored at room temperature. Synthetic lead chromate ($PbCrO_4$), produced via standard chemical methods and purchased from Sigma-Aldrich (Germany), was utilized as a reference for the hazardous material in YTP and is referred to below as "standard $PbCrO_4$". Below, the term $PbCrO_4$ was applied when relating to studies where the crystallinity of the particles was not verified, whereas the term crocoite was used for crystalline $PbCrO_4$ particles in the YTP matrix only. After collection, asphalt that was present within the YTP samples was manually removed with tweezers. All samples were hand ground for 1 min utilizing an agate mortar and pestle in order to obtain a well dispersed powder. Dimensional distributions, determined by environmental scanning electron microscopy (ESEM), were similar for YTP before and after grinding as gentle force was applied to the paint (Fig. S.1.1).

ArcGIS (ESRI Inc., USA), a computer software used for compiling and analyzing geographic data, was utilized to assess the potential volume of YTP in Philadelphia. These calculations were conducted using publicly available data from the City of Philadelphia Streets Department (2015). Two-way streets, which fit the criteria for YTP to be administered, were identified and included in the calculation as all these streets were assumed to be painted. This ArcGIS assessment will provide information for future research and for the potential regulation of YTP.

2.2. Powder X-ray diffraction (PXRD) and X-ray fluorescence (XRF)

Subsequent to producing powders suitable for PXRD, the samples of YTP, asphalt, and standard $PbCrO_4$ were transferred into 16mmdiameter holders. Samples were analyzed using a Panalytical X'Pert Powder X-ray Diffractometer, equipped with an X'Celerator detector and spinning stage, and the resulting patterns processed following the methods described in O'Shea et al. (2020), except that the X-ray patterns were recorded from 5°–90° 2θ and for a total run time of 2 h. After the dissolution experiments, none of the samples could be re-analyzed with PXRD, because not enough material was available.

A Panalytical Epsilon-1 Benchtop XRF Spectrometer was employed on the powdered samples for an initial determination of their elemental composition.

2.3. Optical microscopy

Images were taken of the YTP, asphalt, and standard $PbCrO_4$ samples utilizing a Leica M165 C stereomicroscope (Leica Microsystems, Germany) with a Leica IC80 D camera prior to experimental sample interactions. This imaging was done to gain an initial understanding of the materials in terms of morphology, texture, spatial relationship and agglomeration status prior to laboratory handling as well as to develop our sample preparation approach.

2.4. Batch reactor experiments and inductively coupled plasma-optical emission spectrometry (ICP-OES)

To imitate environmental and human body interactions, we utilized simulated rainwater (ERM-CA408), simulated lung fluid (modified Gamble's solution), and simulated gastric fluid (gastric phase extraction using the Solubility Bioaccessibility Research Consortium assay); in this paper, these fluids are referred to as rainwater, Gamble's solution, and gastric fluid, respectively. The rainwater contains the following components (concentrations in $mg{\cdot}L^{-1}$): NaF, 0.411; Na_2SO_4, 2.045; NH_4Cl, 2.568; $CaN_2O_6{\cdot}4H_2O$, 1.771; $Mg(NO_3)_2{\cdot}6H_2O$, 1.564; $NaNO_3$, 0.331; K_2HPO_4, 0.540; and H_6NO_4P, 0.863. The starting pH of the rainwater was 6.28. The composition of Gamble's solution was similar to that used by Marques et al. (2011) and identical to that used by Vigliaturo et al. (2018); the solution contained the following components (concentrations in $g{\cdot}L^{-1}$): $MgCl_2{\cdot}6H_2O$, 0.203; NaCl, 6.019; KCl, 0.298; Na_2HPO_4, 0.126; Na_2SO_4, 0.063; $CaCl_2{\cdot}2H_2O$, 0.368; $NaC_2H_3O_2{\cdot}3H_2O$, 0.952; $NaHCO_3$, 2.604; and $Na_3C_6H_5O_7{\cdot}2H_2O$, 0.097. This solution was utilized due to its successful application in previous studies (e.g., Marques et al., 2011; Pacella et al., 2014; Vigliaturo et al., 2018). The simulated gastric fluid was composed of 0.4 M glycine (Alfa Aesar, USA) adjusted to pH 1.5 with ACS-grade HCl (Fisher Chemical, USA). This gastric fluid was employed due to its consistency (U.S. EPA, 2007; Deshommes et al., 2012; Ettler et al., 2019); this extraction simulates a fasted human and represents the most high-risk scenario. Interactions with gastric fluid lasted for only one hour, whereas the interactions with rainwater and Gamble's solution lasted for 168 h. YTP (in triplicate), asphalt, and standard $PbCrO_4$ were added to each fluid to a final concentration of 1.25 $mg{\cdot}mL^{-1}$. All solutions were individually mixed using a magnetic stir bar and subsequently pipetted into 10 mL falcon tubes (batch reactors). Batch reactors were then incubated at room temperature (approximately 21 °C) to imitate environmental conditions (rainwater) or 37 °C to simulate human body conditions (Gamble's solution and gastric fluid). None of the batch experiments were exposed to sunlight – the rainwater experiment took place on a lab bench, whereas the Gamble's solution and gastric fluid experiments were carried out in an enclosed incubator. Rainwater and Gamble's solution batch reactors were treated as outlined in Vigliaturo et al. (2018). The batch reactors for rainwater and Gamble's solution were sacrificed at 0, 0.5, 1, 12, 24, 48, 96, and 168 h time points. The gastric fluid batch reactors were sacrificed at 0, 0.5, and 1 h time points. At each time point, sacrificed batch reactors were centrifuged and processed as described in Vigliaturo et al. (2018).

The supernatant solutions for each experiment at every time point were analyzed by ICP-OES (Genesis, Spectro GMBH). The cumulative error of the spectrometer is typically ±2%. The elemental concentrations for Na, Mg, Al, Si, K, Ca, Ti, V, Cr, Mn, Fe, Ni, Zn, and Pb

were determined. Five calibration standards (40 ppm, 20 ppm, 10 ppm, 5 ppm, and 1 ppm) were created for each element utilizing SPEX Certiprep (USA) commercial element standards. All experimental results of ICP-OES analysis are provided in Table S.1.1, but only Pb and Cr are discussed in this manuscript. For quality assurance, the blanks of each fluid were measured before starting the experiments, whereby the concentrations of Pb and Cr were below the detection limit in all cases (<0.013 ppm Pb and <0.003 ppm Cr). All YTP samples were measured in triplicate, and the reported data represent the mean of these three analyses. When graphing the ICP-OES results, five minutes were added to each time point to compensate for time delays in the experimental methods. To calculate the % extracted, the final concentrations of Pb and Cr in solution were compared with their initial concentrations in the starting materials. The latter were taken from the XRF results, because we did not have enough starting YTP material to carry out ICP-OES. The solid residues at the final experimental time points (168 h [rainwater and Gamble's solution] or 1 h [gastric fluid]) were subsequently air dried prior to microscopic analysis.

2.5. ESEM and energy-dispersive X-ray (EDX) spectroscopy

A FEI Quanta 600 FEG Mark II Field Emission ESEM (FEI Company, Hillsboro, OR, USA) was used to investigate the samples (YTP, asphalt, and standard $PbCrO_4$) both before and after exposure to the fluids. We selected one of the triplicate YTP samples before interaction and one sample after final interaction with each fluid (rainwater, Gamble's solution, gastric fluid) for ESEM analysis. We studied the morphology and calculated dimensional distributions for the YTP samples pre- and post-interaction for all three experiments. The samples were mounted on 12.7 mm aluminum stubs with conductive carbon tabs. Pictures were taken in secondary electron (SE) mode, at 1000× magnification with a voltage of 30 kV, and a spot size of 3. We measured the major axis (D) and the minor axis (d) and recorded the morphology for each particle that was assessed. The dimensional parameters λ and s were then calculated, where $\lambda = \frac{D}{d}$ and $s = \sqrt[2]{D \bullet d}$. The s parameter was used because it is not dependent on the 2D-projected particle shape and has identical dimensionality (Kouropis-Agalou et al., 2014). The ellipsoidal volume (V_e)was calculated assuming that the third dimension of the ellipsoid was equal to s, and is expressed by the equation $V_e = \frac{4}{3} \cdot \pi \cdot D \cdot d \cdot s$. The equivalent-volume diameter was calculated according to: $D_{ev} = \left(\frac{6}{\pi} V_e\right)^{\frac{1}{3}}$, which is the diameter of a sphere—the same volume of the considered particle. Surface area (S_A) of individual particles was calculated with $S_A = 4 \cdot \pi \left(\frac{(D \cdot d)^{1.6} + (D \cdot s)^{1.6} + (d \cdot s)^{1.6}}{3} \right)^{\frac{1}{1.6}}$. This method was chosen because two dimensions (D, d) were measured on the ESEM and s was used to estimate thickness. The calculated descriptive statistics included the mean, standard deviation (σ_{n-1}), minimum value (min), and maximum value (max). All values were obtained by measuring 100 particles per sample. Standard deviation of the mean is simply referred to as standard deviation in this paper. A power law fitting of our experimental data was applied.

ESEM-EDX chemical analysis was performed on 20 spots per sample, with the above conditions but with a magnification of 20,000× and a spot size of 6. We focused on regions with Pb and Cr signals, which indicated the presence of crocoite particles. The Pb/Cr value, using atomic percent (at.%), was used to track chemical modifications in the investigated material.

2.6. Scanning/transmission electron microscopy (S/TEM) and EDX spectroscopy

Samples of the YTP were analyzed using S/TEM both before and after exposure to the fluids. We selected one of the triplicate YTP samples before interaction and one sample after final interaction with each fluid (rainwater, Gamble's solution, gastric fluid) for S/TEM analysis. A small amount of pre-interaction YTP was suspended in 1 mL of clean Milli-Q water within an Eppendorf tube. Samples were vigorously shaken, and a droplet was placed onto a 200-mesh copper grid (SPI 2020C) and allowed to air dry; a second droplet was placed over the first grid once the grid had dried. The same procedure was used for YTP after interaction with simulated rainwater, lung, and gastric fluids. A JEM-F200 Multipurpose Analytical S/TEM equipped with a cold-field emission gun operating at 200 kV and two large-area energy-dispersive X-ray spectrometers was utilized. High-resolution S/TEM, in combination with fast-Fourier transform (FFT) and selected area electron diffraction (SAED), was used to determine the degree of particle crystallinity. STEM-EDX mapping was performed to detect, characterize, and define the spatial location of crocoite particles in the YTP, previously localized using ESEM. The STEM-EDX spectra were obtained in regions of interest containing crocoite particles. The background was subtracted from the STEM-EDX spectra to remove thickness effects. All post-interaction S/TEM images were taken at the final experimental time points.

3. Results

3.1. Pre-interaction results

3.1.1. YTP volume—The potential volume of YTP present in Philadelphia was calculated by analyzing all 4548 km of 40,659 streets. 22,075 of the streets are two-way and made up a total length of 2486 km. A lower and upper estimate for the YTP width was created based on the typical width of the paint stripes (100–150 mm) (Federal Highway Administration, 2000). All two-way streets were calculated as having 2 continuous yellow paint stripes. The average thickness for US road markings is 2 mm (e.g., Naidoo and Steyn, 2018). From these data, the total volume of YTP used in Philadelphia was calculated as between 994 and 1492 m^3. Utilizing the upper and lower volume calculations above and our XRF data, we estimate that 59.8–89.5 t Pb and 12.5–18.8 t Cr are spread across Philadelphia in the form of YTP. This estimate was calculated using a YTP density of 1.63 g/mL (Alabama Department of Transportation, 2008), as we do not know the exact density of Philadelphia YTP.

3.1.2. PXRD and XRF—Analysis of the PXRD patterns (example shown in Fig. S.1.2) revealed the presence in YTP of the following crystalline phases and their estimated abundances (in parentheses): calcite (70 wt%), dolomite (14 wt%), crocoite (5 wt%), rutile (4 wt%), and quartz (1 wt%). The detected crystalline phases in asphalt were albite (70 wt

%), dolomite (23 wt%), and quartz (7 wt%). The only phase identified in standard $PbCrO_4$ was crocoite (Table 1).

When using the bulk elemental concentrations in the samples (determined by XRF), the atomic ratios of Pb to Cr in YTP (1.20) and standard $PbCrO_4$ (1.23) were similar (Table 2).

3.1.3. Light microscopy—The YTP particles were heterogenous in size, generally bright orange-yellow in color, massive in texture, and had visible glass beads present (Fig. 1a, b). In the following, YTP particles are defined as heterogenous mixtures that contain two or more of the following constituents: polymers, crocoite, asphalt, glass spheres, and rutile. The asphalt was also heterogeneous in size and color (primarily black, grey, and white) and had a fine-grained texture (Fig. 1c). Standard $PbCrO_4$ displayed a vivid orange color and occurred as aggregates with variable particle sizes (Fig. 1d).

3.1.4. ESEM-EDX—YTP particles exhibited a mean D of 11.9 ± 11.0 μm and a mean d of 6.0 ± 6.8 μm(Table 3). The s parameter can be fit well ($R^2 = 0.93$) with a power law function (Fig. S.2.1). The mean s value for YTP particles was 8.3 ± 8.3 μm (Table 3). The average S_A of these particles was 1834 μm^2, with a considerable range in values (36,244 μm^2 to 14 μm^2). The average V_e of the YTP particles was 2173 μm^3, with a range from 80,410 μm^3 to 0.5 μm^3. The most common morphology was equant (37%) (Table 3, Fig. S.2.2). The term "equant" refers to particles that have nearly equal values of D and d (Veblen and Wylie, 1993). Other shapes present, as defined by Campbell (1977) and Veblen and Wylie (1993), were: massive, bladed, acicular, lamellar, platy, prismatic, fibrous, and columnar (Fig. S.2.2). Only the most abundant shapes are discussed herein. When viewed under ESEM, the YTP particles appeared to consist of many aggregated particles embedded in a Ca-rich matrix (Fig. 2) and these particles displayed a range of sizes (Fig. S.2.3). The Si- and O-rich area in Fig. 2 is a glass bead approximately 400 μm in diameter – comparable to the roughly 250 μm diameter bead in Fig. 1b. The areas containing both Pb and Cr (inferred to be crocoite) in YTP particles appeared as distinct phases in the matrix (Fig. S.2.4), as also seen in the element distribution images in Fig. 2.

Using ESEM-EDX spot analysis, the average Pb/Cr values in YTP particles (n = 20) and standard $PbCrO_4$ (n = 20) were 0.95 and 1.00, respectively, i.e. close to the ideal 1.00, although standard $PbCrO_4$ had a high estimated total error (0.22) (Fig. 3).

3.1.5. S/TEM-EDX—Element mapping of YTP particles by STEM-EDX revealed that Pb and Cr were concentrated at the same locations, which correspond to the dark-contrast grains in the bright-field TEM images and thus represent crocoite particles (see Fig. 4a). This interpretation is also consistent with the information gathered from the PXRD patterns. On the other hand, Ti- and Si-rich particles were spatially separated from each other and concentrated in individual, rounded phases (Fig. 4a) which, based on the information obtained from the PXRD patterns, must be rutile and quartz. Silicon, however, also occurs as coatings around crocoite particles (Fig. 4a, see also Fig. S.3.1a). Unlike the crocoite particles, which are crystalline, these rims are amorphous, as documented by FFT diffraction patterns (Fig. S.3.2). These amorphous coatings also contain O, and therefore are referred to as a silica coating below (Fig. S.3.3). The value of D for these coated crocoite particles

ranged from 0.5 μm to 0.2 μm, that of *d* from0.3 μm to 0.2 μm (Table S.3.1). These ranges were almost identical to those of standard $PbCrO_4$ (*D*: 0.4–0.2 μm; *d*: 0.3–0.1 μm). The standard $PbCrO_4$, however, did not show a silica coating (Fig. S.3.4). An electron-beam stability test was performed on standard $PbCrO_4$ and it demonstrated the stability of the material at the instrument conditions used (Fig. S.3.4).

3.2. Post-interaction results: environment

3.2.1. Rainwater: ESEM-EDX—After interaction with rainwater, the mean *D* (6.7 ± 6.1 μm) and *d* (3.3 ± 2.6 μm) values of YTP particles were smaller than the corresponding pre-interaction values (Table 3). On the other hand, the *s* power law function was similar, but the fit was less robust (Fig. S.2.1). The mean *s* value (4.6 ± 3.6 μm) was smaller than the corresponding value of the original material. The ranges in S_A (4523–3 μm^2) and V_e (2130–0.1 μm^3) were also smaller than those of the corresponding starting material. After interaction with rainwater, most parameters were within one standard deviation of the corresponding starting material values. As with the pre-interaction YTP particles, the most frequent morphology observed was equant (48%) (Table 3, Fig. S.2.2). The Pb/Cr value of YTP particles (1.12) (n = 20) after interaction with rainwater was similar to that of the original material value (0.95), albeit with a much larger estimated total error (Fig. 3). Overall, ESEM images qualitatively indicated that the YTP particles appeared to be more rounded after their interaction with rainwater (Fig. S.2.3).

3.2.2. Rainwater: S/TEM-EDX—Subsequent to the YTP interaction with rainwater, bright-field TEM images and STEM-EDX element distribution maps highlighted areas with collocated Pb and Cr signals, which were inferred to be crocoite particles. These particles were similar to those observed in the pre-interaction images (Fig. 4b). Their crystallinity was not altered (Fig. S.3.5). Moreover, their silica coating persisted during interaction with rainwater (Fig. 4b). In one case, the Pb and Cr signals appeared to be present throughout the YTP-particle matrix (Fig. S.3.1b). The dispersed signals observed in the matrix were less intense and less localized than those concentrated on crocoite particles (Fig. S.3.1b).

3.2.3. Rainwater: ICP-OES—For YTP particles, no Pb or Cr were detected in rainwater at any of the time points, except for Pb and Cr at the first time point, where mean concentrations of 0.014 ppm Pb and 0.005 ppm Cr, were measured (Fig. 5; Table S.1.1). For asphalt, no Pb or Cr were detected in rainwater at any time point. For the case of standard $PbCrO_4$, Pb was immediately released to 0.031 ppm and then increased to a final concentration of 0.152 ppm (Fig. 5a). From standard $PbCrO_4$, Cr was immediately released to 0.27 ppm, from where its concentration increased in a time-dependent fashion, modeled by a power law fit with an R^2 value of 0.99, to a final concentration of 1.027 ppm (Fig. 5b). At the endpoint of the rainwater interaction with standard $PbCrO_4$, the extractable Pb and Cr values were 0.02% and 0.75%, respectively (Table 4).

3.3. Post-interaction results: simulated body fluids

3.3.1. Gamble's solution and gastric fluid: ESEM-EDX—After interaction with Gamble's solution, the mean *D* (7.3 ± 6.9 μm) and *d* (3.7 ± 3.0 μm) values of the YTP particles were smaller than the corresponding values in the starting material (Table 3). In

contrast, the s power law function was similar to the corresponding functions determined for the YTP particles both before and after interaction with rainwater (Fig. S.2.1). The mean s value was 5.1 ± 4.4 μm, which was lower than the corresponding value of the original material but similar to the one observed after interaction with rainwater. The ranges in S_A (7454 – 2 μm^2) and V_e (6586–0.1 μm^3) were smaller than the corresponding ranges of the original material. The most frequent morphology was equant (68%) (Table 3, Fig. S.2.2). The Pb/Cr value of YTP particles (1.01) after interaction with Gamble's solution was similar to the corresponding value of the starting material (Fig. 3).

After gastric-fluid interaction, the mean D (11.9 ± 13.4 μm) and d (5.2 ± 5.7 μm) values of the YTP particles were slightly smaller than the corresponding pre-interaction values (Table 3), whereas the s power law function was similar (Fig. S.2.1). The mean s value (7.7 ± 8.5 μm) was slightly lower than the corresponding value in the original material. The ranges in S_A (35,654–3 μm^2) and V_e (71,872–0.1 μm^3) were similar to those of the starting materials. Again, the most common morphology was equant (53%) (Table 3, Fig. S.2.2). The Pb/Cr value of YTP particles (0.93) after interaction with gastric fluid was close to that of the original material (Fig. 3).

3.3.2. Gamble's solution and gastric fluid: S/TEM-EDX—Subsequent to the YTP interaction with Gamble's solution, areas with Pb and Cr signals were collocated and were inferred to be crocoite particles, as in the starting material (Figs. 4c, S.3.1c). Their silica coating also persisted during interaction with Gamble's solution (Figs. 4c, S.3.6). Again, in some cases, Pb and Cr signals were dispersed throughout the YTP particle matrices (Fig. S.3.1c).

After the YTP interaction with gastric fluid, the Pb and Cr maps and the STEM images were nearly identical to the corresponding images of the starting material (Fig. 4d). The crocoite particles (according to PXRD data) and their silica coatings persisted during their interaction with gastric fluid (Figs. 4d, S.3.7). Lead and Cr signals were dispersed throughout some of the YTP particle matrices (Fig. S.3.1d).

3.3.3. Gamble's solution and gastric fluid: ICP-OES—In Gamble's solution, Pb was not released from any of the three studied materials at any time point except for the first time point, where concentrations of 0.020 ppm and 0.013 ppm were measured for YTP particles and standard $PbCrO_4$, respectively (Fig. 6a). From standard $PbCrO_4$, Cr was immediately released to 0.57 ppm and then increased, modeled by a power law fit with a low R^2 value (0.52), to a final concentration of 0.86 ppm (Fig. 6b). These values correspond to 0.42% and 0.63% extractable Cr, respectively (Table 4). In the cases of YTP particles and asphalt, Cr was not detectable at any time point except for the first time point, where 0.017 ppm was measured for YTP particles (Fig. 6b).

In gastric fluid, Pb from YTP particles was immediately released to 0.30 ppm and then increased to a final concentration of 0.43 ppm (Fig. 7a). From asphalt, Pb was immediately released to 0.04 ppm and had a nearly identical final concentration. On the other hand, from standard $PbCrO_4$, Pb was immediately released to 56.91 ppm and then increased to a final concentration of 69.18 ppm. These values correspond to 8.48% and 10.31% extractable Pb,

respectively (Table 4). From YTP particles, Cr was immediately released to 0.05 ppm and slightly increased to a final concentration of 0.09 ppm (Fig. 7b). From asphalt, Cr was immediately released to 0.007 ppm but was not detectable in the final solution (<0.003 ppm). From standard $PbCrO_4$, Cr was immediately released to 14.86 ppm and then increased to a final concentration of 18.01 ppm. These values corresponded to 10.84% and 13.14% extractable Cr, respectively (Table 4).

4. Discussion

4.1. Pre-interaction

The mineral phases found in Philadelphia's YTP particles (Table 1) were similar to those identified in YTP from Hamilton, Ohio (White et al., 2014) and Hermosillo, Mexico (Meza-Figueroa et al., 2018; González-Grijalva et al., 2019). However, the Hermosillo studies documented a significant quantity of kaolinite and did not report dolomite, reflecting the local soils. All phases found in the Philadelphia YTP particles, except for dolomite, were found in Hamilton. In Hamilton, a variety of locations were tested and some YTP particles contained crocoite whereas others did not. These results demonstrated that YTP used within the same city can be mineralogically heterogeneous (White et al., 2014).

We documented a silica coating of crocoite in YTP particles from Philadelphia (e.g., Figs. 4a; S.3.1; S.3.2; S.3.3). The crocoite in YTP particles had nearly identical maximum and minimum D and d values to the corresponding values for standard $PbCrO_4$. Previous studies have shown that amorphous silica has a low solubility in water and only becomes more soluble at pH conditions that are higher than those we tested (Alexander et al., 1954). In a study performed in Daejeon, South Korea, a silica-bearing layer also surrounded the $PbCrO_4$ pigments in the YTP samples (Lee et al., 2018). Our Pb, Si, and Cr maps of YTP particles, obtained by STEM-EDX, were comparable to the corresponding elemental maps from the Daejeon study. Due to these similarities, our YTP study is relevant to cities worldwide.

4.2. Post interaction (environment)

During interaction with rainwater, the YTP particles experienced a trend towards dimensional reduction (not statistically significant) related to the probable loss of particle agglomeration (Table 3; Fig. S.2.3). The crocoite particles remained crystalline throughout this interaction (Fig. S.3.5). The Pb and Cr signals in STEM-EDX maps were mostly concentrated in these crocoite particles (Fig. 4b), some cases were also dispersed throughout the matrix of the YTP particles (Fig. S.3.1b). These diffuse elemental signals indicate that some Pb and Cr may have been mobilized from the crocoite particles and subsequently trapped by the surrounding polymer matrix and, thus, did not leave the YTP particle itself. In some particles, Pb is concentrated in certain spots, whereas the Cr is dispersed across the entire particle (Fig. S.3.1b), which is not fully understood at this moment (see below).

One potential reason why minute amounts of Pb (0.014 ppm) and Cr (0.005 ppm) were initially released from the YTP particles, as well as from standard $PbCrO_4$, may be that these elements were desorbed from the surface of the particles upon first exposure to rainwater. These initial concentrations were extremely small, but higher than in the blanks (Pb and Cr

were both not detected in the pure rainwater). At all other time points, including the endpoint of the experiment, the concentrations of both Pb (Fig. 5a) and Cr (Fig. 5b) were below the detection limits (Pb < 0.013 ppm; Cr < 0.003 ppm) in the solutions resulting from the YTP-rainwater interaction. In the case of standard $PbCrO_4$, however, both metals were detected at the endpoint of rainwater interaction (Pb = 0.152 ppm; Cr = 1.027 ppm; Fig. 5a,b). Future experiments on standard $PbCrO_4$ are required to better understand why Pb was only detected at the first and last timepoints. Recalculating the final values into molar units yields final concentrations of 7.34×10^{-7} M for Pb and 8.85×10^{-6} M for Cr (expressed as CrO_4^{2-}). Crocoite has a low solubility of 1.79×10^{-7} M in pure water at 25 °C (e.g., Centers for Disease Control and Prevention (CDC), 2012; Beauchemin et al., 2011). This value is comparable to the final concentration of Pb determined in the rainwater solution after interaction with standard $PbCrO_4$, but is one order of magnitude lower than the final concentration of Cr. This discrepancy, thus, points to incongruent dissolution of the standard material in rainwater.

On the other hand, the Pb/Cr ratio determined by ESEM/EDX for the standard $PbCrO_4$ particles after exposure appears smaller (albeit statistically insignificant) than the stoichiometric value of 1.00 exhibited before interaction (Fig. 3), which indicates the opposite behavior, i.e. preferential removal of Pb. A possible explanation for this discrepancy is that the signal for the ESEM/EDX spot analysis results primarily from the bulk of the crocoite particles, because of the comparatively large volume of interaction of the electron beam, thus not allowing us to detect potential surface modifications.

Incongruent dissolution of crocoite was reported also by White et al. (2014), who studied the behavior over one month of crocoite in solutions containing various concentrations of NaCl or $CaCl_2$. These authors, however, detected Pb, but not Cr in all of their solutions, and they observed that the Pb concentrations increased with increasing salinity, whereby the reported Pb values, in all cases, were higher than the final Pb concentration we observed in our experiment with rainwater and standard $PbCrO_4$. Another previous study of $PbCrO_4$ pigments (Gao et al., 2019) found that after a 7-h exposure in natural sunlight to river water (pH = 6.21), the Pb^{2+} concentrations in solution were more than three times higher than those of Cr^{3+} (approximately 1.5×10^{-6} M; trivalent Cr due to the presence in the water of 6.14 mg/L total organic carbon), which were similar to the Cr concentration we measured at the end of our experiment with rainwater. The differences between our results and those of previous studies may be due to varying length of experiments, composition of fluids, and overall difference in experimental variables (e.g., use of sunlight). Overall, these diverse results imply the need for additional systematic dissolution studies of $PbCrO_4$ pigments.

The observed retention of both Pb and Cr within the YTP particles during the interaction with rainwater could be due to the silica coating of the crocoite particles. These coatings persisted during the experiment and probably inhibited crocoite dissolution. This conclusion is supported by a previous study (Pier et al., 1991), which reported that the solubility of $PbCrO_4$ pigments in simulated environmental conditions was lower when they were coated with amorphous silica compared to when they lacked the coating. These results highlight the importance of the silica coating of crocoite in protecting the pigment from dissolution. On

the other hand, such coatings can be degraded in real environmental conditions (Lee et al., 2018), which might lead to enhanced release of Pb and Cr.

The retention of Pb and Cr within the YTP particles observed in our experiments could also result from the presence of the polymer matrix that embed the silica-coated crocoite. These YTP polymers probably further limited the interaction between the coated crocoite and the rainwater.

4.3. Post interaction (body)

The size of YTP particles decreased after interaction with Gamble's solution, documenting a trend towards dimensional reduction (albeit not statistically significant) (Table 3, Fig. S.2.3). This result suggests that the YTP particles, once inhaled, may experience a particle size reduction (deagglomeration) during their interaction with the lung fluid, allowing the particles to go deeper into the lungs. Eventually, the particles could reach the trachea-bronchial region of the lungs due to their mean size (s = 5.1 μm) (e.g., Kastury et al., 2017) (Table 3). Additionally, the deagglomeration of the YTP particles may liberate the individual crocoite particles (D: 0.3 μm; d: 0.2 μm) from the surrounding polymer matrix during interaction. These liberated, small crocoite particles could eventually reach the alveolar region of the lungs (e.g., Kastury et al., 2017), (Table S.3.1). On the other hand, the size of the YTP particles was statistically not significantly different after interaction with the gastric fluid (Table 3).

The crocoite particles remained crystalline after interaction with both Gamble's solution and gastric fluid (Figs. S.3.6; S.3.7). As was also described for rainwater interaction, in some cases, we observed that the Pb and Cr STEM-EDX signals were dispersed throughout the YTP particle matrix after both gastric fluid and Gamble's solution interaction (Fig. S.3.1c,d).

The ICP-OES data showed that the YTP particles did not release detectable amounts of Pb and Cr into Gamble's solution at the endpoint of the experiment (Fig. 6). Lead and Cr were only detected at the first time point, an observation that may, as mentioned for rainwater, be explained by initial desorption of metals from the surface of the particles. This may also apply to the interaction with standard $PbCrO_4$ and to all of the initial gastric fluid interactions. At the end of the experiment with standard $PbCrO_4$, no Pb was detected in Gamble's solution, but Cr was present in a concentration of 0.858 ppm, which corresponds to 7.40×10^{-6} M Cr (expressed at CrO_4^{2-}) and is similar to the concentration observed in rainwater (8.85×10^{-6} M). As was the case with rainwater, these data point to incongruent dissolution of standard $PbCrO_4$ in Gamble's solution. However, the Pb/Cr ratio in standard $PbCrO_4$, calculated from ESEM/EDX spot analyses, is close to the stoichiometric value of 1.00 and, therefore, points to congruent dissolution.

In gastric fluid, Pb and Cr were released from YTP particles to detectable concentrations at all three time points (Fig. 7). The final Pb (0.43 ppm) and Cr (0.09 ppm) values correspond to 2.10×10^{-6} M Pb and 7.82×10^{-7} M Cr (expressed as CrO_4^{2-}). The lower pH (1.5) of the gastric fluid compared to that of the Gamble's solution (7.4) could help to account for the

differences in ICP-OES values (e.g., Fraser and Fairhall, 1959). Also, Gamble's solution contains a variety of components that are not present in gastric fluid, which could also affect the release of Pb and Cr. For the case of asphalt, the detectable concentrations of Pb (at all time points) and Cr (first time point) found in gastric fluid could be sourced from road dust coating the particles (e.g., O'Shea et al., 2020). In the case of standard $PbCrO_4$, the concentrations of Pb and Cr at the end of the experiment with gastric fluid were 69.18 ppm Pb (3.34×10^{-4} M) and 18.01 ppm Cr (1.55×10^{-4} M, expressed as CrO_4^{2-}). These final values suggest that the dissolution of standard $PbCrO_4$ was nearly congruent in gastric fluid, thus contrasting with the results obtained from the experiments with rainwater and Gamble's solution. This conclusion is also consistent with the Pb/Cr values for standard $PbCrO_4$ after gastric-fluid interaction, which were close to the stoichiometric value of 1.00.

The amounts of Pb and Cr extractable by gastric fluid were 10.31% and 13.14%, respectively for standard $PbCrO_4$, but only <1% for the studied YTP particles (Table 4). These data indicate that crocoite particles that are coated by an amorphous silica layer and embedded in the paint polymer matrix pose a lower risk to human health than uncoated pure $PbCrO_4$ (see also Levy et al., 1986; Pier et al., 1991).

5. Conclusions

The experiments performed in this study generated a more detailed understanding of a topic of growing concern: YTP pollution. Our multi-analytical approach provided an in-depth characterization of YTP, and we recommend it for use in future investigations.

After most experimental interactions, particles tended to be smaller, although the dimensional reductions were not statistically significant. In agreement with previous studies, our data document that the coated crocoite particles in YTP are persistent during the experimental interactions and that they are probably less dangerous than initially believed, as they released much smaller amounts of Pb and Cr into the tested solutions than the uncoated standard $PbCrO_4$. In addition, the coated crocoite particles in YTP are surrounded by the paint polymers which further protect the crystals from dissolving and buffer the release of Pb and Cr into final solution by trapping the metals.

S/TEM is the only technique that can clearly identify the presence of the silica coatings surrounding crocoite particles. Since this technique is costly, time-consuming, and difficult to access, we recommend that municipalities utilize alternative traffic paints, which are Pb- and Cr-free and thus do not contain $PbCrO_4$ pigments. While Pb is banned in residential and toy usage in the US, it is still used in commercial and traffic settings.

Our experiments offer the first step in better understanding the chemical and morphologic evolution of YTP particles containing coated crocoite in conditions that simulate human body and environmental exposures. Future studies are required to understand under what conditions and time scales the coatings break down. We did not consider factors such as soils, organics, road salting or treatment, potential carbonation, valence states, or the state of the paint (e.g., flaked). Furthermore, we did not examine the role or behavior of elements other than Pb and Cr present in YTP (e.g., Ca, Ti, Mg) during dissolution, which was

beyond the scope of our study; the data for these additional elements, however, are reported in Table S.1.1 (Supplemental Material). We only investigated one single site in Philadelphia. It is possible that there are YTP samples in the city where a silica coating is not present around crocoite particles or where other yellow pigments were used. We suggest that future studies sample multiple areas throughout cities in order to account for this possible variation. Moreover, future investigations should test YTP in additional biological fluids, such as, intestinal solutions and artificial lysosomal fluid. New inquiries should also consider incorporating techniques such as wavelength-dispersive spectroscopy (WDS) to acquire additional analytical information. Using WDS will allow researchers to better assess the relatively large estimated total error of the mean Pb/Cr value in YTP after experimental interactions (Fig. 3). Our study suggests the need for systematic investigations of the dissolution and stability of crocoite pigments under a wider variety of appropriate environmental and human body conditions. Finally, due to the large amount of crocoite on the streets of Philadelphia, the consequences of long-term rainwater exposure must be considered in the future.

Supplementary Material

Refer to Web version on PubMed Central for supplementary material.

Acknowledgements

We thank the Benjamin Franklin Fellowship and the Greg and Susan Walker Foundation for support from the University of Pennsylvania. This work was further supported by the U.S. National Institute of Environmental Health Sciences (NIEHS) grant P30-ES013508, awarded to the University of Pennsylvania. The findings are not the official opinions of NIEHS or NIH. We deeply thank the reviewers and the editor of our manuscript for their assistance with improving this work.

References

Adachi K, Tainosho Y, 2004 Characterization of heavy metal particles embedded in tire dust. Environ. Int 30, 1009–1017. [PubMed: 15337346]

Agency for Toxic Substances and Disease Registry (ATSDR), 2012 Toxicological Profile for Chromium. U.S. Department of Health and Human Services, Public Health Service, Atlanta, GA.

Agency for Toxic Substances and Disease Registry (ATSDR), 2017 ATSDR's Substance Priority List. U.S. Department of Health and Human Services, Public Health Service, Atlanta, GA.

Agency for Toxic Substances and Disease Registry (ATSDR), 2019 Toxicological Profile for Lead. (Draft for Public Comment). U.S. Department of Health and Human Services, Public Health Service, Atlanta, GA.

Alabama Department of Transportation, 2008 Retroreflective Roadway Markings for all Weather Conditions. Maintenance Bureau, Montgomery, Alabama.

Alatise OI, Schrauzer GN, 2010 Lead exposure: a contributing cause of the current breast cancer epidemic in Nigerian women. Biol. Trace Elem. Res 136, 127–139. 10.1007/s12011-010-8608-2. [PubMed: 20195925]

Alexander GB, Heston WM, Iler RK, 1954 The solubility of amorphous silica in water. J. Phys. Chem-US 58, 453–455.

Alexeeff GV, Satin K, Painter P, Zeise L, 1989 Chromium Carcinogenicity: California Strategies. vol. 86 The California Department of Health Services (CDH), pp. 159–168.

Anderson RA, 1998 Chromium, glucose intolerance and diabetes. J. Am. Coll. Nutr 17, 548–555. 10.1080/07315724.1998.10718802. [PubMed: 9853533]

Anttila A, Heikkila P, Pukkala E, Nykyri E, Kauppinen T, Hernberg S, Hemminki K, 1995 Excess lung cancer among workers exposed to lead. Scand. J. Work. Environ. Hlth 21, 460–469. 10.5271/sjweh.62.

Bavec Š, Biester H, Gosar M, 2014 Urban sediment contamination in a former Hg mining district, Idrija, Slovenia. Environ. Geochem. Health 36, 427–439. 10.1007/s10653-013-9571-6. [PubMed: 24114255]

Beauchemin S, MacLean LCW, Rasmussen P, 2011 Lead speciation in indoor dust: a case study to assess old paint contribution in a Canadian urban house. Environ. Geochem. Health 33, 343–352. 10.1007/s10653-011-9380-8. [PubMed: 21465232]

Bi X, Li Z, Sun G, Liu J, Han Z, 2015 In vitro bioaccessibility of lead in surface dust and implications for human exposure: a comparitive study between industrail area and urban district. J. Hazard. Mater 297, 191–197. 10.1016/j.jhazmat.2015.04.074. [PubMed: 25958267]

Campbell WJ, 1977 Selected Silicate Minerals and their Asbestiform Varieties: Mineralogical Definitions and Identification-Characterization, Volume 8751 of Information Circular - Bureau of Mines, United States Bureau of Mines.

CDC, 2012 International Chemical Safety Cards (ICSC). Centers for Disease Prevention & Control. National Institute for Occupational Safety & Health (NIOSH), Atlanta, GA.

Charlesworth S, De Miguel E, Ordonez A, 2011 A review of the distribution of particulate trace elements in urban terrestrial environments and its application to considerations of risk. Environ. Geochem Hlth 33, 103–123. 10.1007/s10653-010-9325-7.

Chon HT, Kim KW, Kim JY, 1995 Metal contamination of soils and dusts in Seoul metropolitan city, Korea. Environ. Geochem. Hlth 17, 139–146.

City of Philadelphia Street Department, 2015 "Track streets". Scale not given. "DVRPC traffic count viewer". 9 21 https://www.opendataphilly.org/dataset/track-streets.

Collins BJ, Stout MD, Levine KE, Kissling GE, Melnick RL, Fennell TR, Walden R, Abdo K, Pritchard JB, Fernando RA, Burka LT, Hooth MJ, 2010 Exposure to hexavalent chromium resulted in significantly higher tissue chromium burden compared with trivalent chromium following similar oral doses to male F344/N rats and female B6C3F1 mice. Toxicol. Sci 118, 368–379. 10.1093/toxsci/kfq263. [PubMed: 20843897]

Council on Environmental Health, 2016 Prevention of childhood Lead toxicity. Pediatrics 138 (1), 1–15. 10.1542/peds.2016-1493.

Datko-Williams L, Wilkie A, Richmond-Bryant J, 2014 Analysis of U.S. soil lead (Pb) studies from 1970 to 2012. Sci. Total Environ 468–469, 854–863. 10.1016/j.scitotenv.2013.08.089.

Deshommes E, Tardif R, Edwards R, Sauvé S, Prévost M, 2012 Experimental determination of the oral bioavailability and bioaccessibility of lead particles. Chem. Cent. J 6, 138 10.1186/1752-153X-6-138. [PubMed: 23173867]

Dietrich M, Huling J, Krekeler MPS, 2018 Metal pollution investigation of Goldman Park, Middletown Ohio: evidence for steel and coal pollution in a high child use setting. Sci. Total Environ 618, 1350–1362. [PubMed: 29111254]

Dietrich M, Wolfe A, Burke M, Krekeler MPS, 2019 The first pollution investigation of road sediment in Gary Indiana: anthropogenic metals and possible health implications for a socioeconomically disadvantaged area. Environ. Int 128, 175–192. [PubMed: 31059913]

Duong TT, Lee BK, 2011 Determining contamination level of heavy metals in road dust from busy traffic areas with different characteristics. J. Environ. Manag 92 (3), 554–562. 10.1016/j.jenvman.2010.09.010.

Ettler V, Cihlová M, Jarošíková A, Mihaljevič M, Drahota P, Kříbek B, Vaněk A, Penížek V, Sracek O, Klementová M, Engel Z, Kamona F, Mapani B, 2019. Oral bioaccessibility of metal(loid)s in dust materials from mining areas of northern Namibia. Environ. Int 124, 205–215. 10.1016/j.envint.2018.12.027. [PubMed: 30654327]

Federal Highway Administration, 2000 Manual on Uniform Traffic Control Devices 2000. U.S. Department of Transportation.

Fraser DA, Fairhall LT, 1959 Lead dissolution from red-lead paints in water. American Water Works Association 51, 561–569.

Gaberšek M, Gosar M, 2018 Geochemistry of urban soil in the industrial town of Maribor, Slovenia. J. Geochemical Explor 187, 141–154. 10.1016/j.gexplo.2017.06.001.

Gao H, Wei P, Liu H, Long M, Fu H, Qu X, 2019 Sunlight-mediated lead and chromium release from commercial lead chroamte pigments in aqueous phase. Envir. Sci. Tech 53, 4931–4939.

González-Grijalva B, Meza-Figueroa D, Romero FM, Robles-Morúa A, Meza-Montenegro M, García-Rico L, Ochoa-Contreras R, 2019 The role of soil mineralogy on oral bioaccessibility of lead: implications for land use and risk assessment. Sci. Total Environ 657, 1468–1479. 10.1016/j.scitotenv.2018.12.148. [PubMed: 30677913]

Gottesfeld P, 2015 Time to ban lead in industrial paints and coatings. Front. Public Health 3, 144 10.3389/fpubh.2015.00144. [PubMed: 26042214]

Gottesfeld P, Pokhrel D, Pokhrel AK, 2014 Lead in new paints in Nepal. Environ. Res 132, 70–75. 10.1016/j.envres.2014.03.036. [PubMed: 24742730]

Haney JT, Erraguntla N, Sielken RL, Valdez-Flores C, 2014 Development of an inhalation unit risk factor for hexavalent chromium. Regul. Toxicol. Pharmacol 68, 201–211. 10.1016/j.yrtph.2013.12.005. [PubMed: 24361343]

Holecy EG, Mousavi A, 2012 Lead sources, toxicity, and human risk in children of developing countries: a mini-review. Environ. Forensic 13, 289–292.

International Agency For Research on Cancer, 2006 Inorganic and Oranic Lead Compounds. Monographs on the Evaluation of Carcinogenic Risks to Humans. vol. 87 WHO, Lyon, France, pp. 1–529.

Jeffs R, Jones W, 1999 Additives for paint Paint and Surface Coatings: Theory and Practice. Woodhead Publishing, Cambridge, pp. 185–197.

Kastury F, Smith E, Juhasz AL, Gan J, 2017 A critical review of approaches and limitations of inhalation bioavailability and bioaccessibility of metal(loid)s from ambient particulate matter or dust. Sci. Total Environ 574, 1054–1074. 10.1016/j.scitotenv.2016.09.056. [PubMed: 27672736]

Kouropis-Agalou K, Liscio A, Treossi E, Ortolani L, Pugno NM, Palermo V, 2014 Fragmentation and exfoliation of 2-dimensional materials: a statistical approach. Nanoscale 6, 5926–5933. [PubMed: 24759898]

Laidlaw MAS, Filippelli GF, 2008 Resuspension of urban soils as a persistent source of lead poisoning in children: a review and new directions. Appl. Geochem 23, 2021–2039. 10.1016/j.apgeochem.2008.05.009.

Laidlaw MAS, Taylor MP, 2011 Potential for childhood lead poisoning in the inner cities of Australia due to exposure to lead in soil dust. Eviron. Pollut 159, 1–9. 10.1016/j.envpol.2010.08.020.

Lanphear BP, Matte TD, Rogers J, Clickner RP, Dietz B, Bornschein RL, Succop P, Mahaffey KR, Dixon S, Galke W, Rabinowitz M, Farfel M, Rohde C, Schwartz J, Ashley P, Jacobs DE, 1998 The contribution of lead-contaminated house dust and residential soil to children's blood lead levels: a pooled analysis of 12 epidemiologic studies. Environ. Res 79, 51–68. 10.1006/enrs.1998.3859. [PubMed: 9756680]

Lee PK, Yu S, Chang HJ, Cho HY, Kang M, Chae B, 2016 Lead chromate detected as a source of atmospheric Pb and Cr (VI) pollution. Nat. Publ. Gr, 1–10 10.1038/srep36088.

Lee PK, Chang HJ, Yu S, Chae KH, Bae JH, Kang MJ, Chae G, 2018 Characterization of Cr (VI) – containing solid phase particles in dry dust deposition in Daejeon, South Korea. Environ. Pollut 243, 1637–1647. 10.1016/j.envpol.2018.09.127. [PubMed: 30296760]

LeGalley E, Widom E, Krekeler MPS, Kuentz DC, 2013 Chemical and lead isotope constraints on sources of metal pollution in street sediment and lichens in Southwest Ohio. Appl. Geochem 32, 195–203. 10.1016/j.apgeochem.2012.10.020.

Leonard SS, Roberts JR, Antonini JM, Castranova V, Shi X, 2004 PbCrO4 mediates cellular responses via reactive oxygen species. Mol. Cell. Biochem 255, 171–179. 10.1023/B:MCBI.0000007273.23747.67. [PubMed: 14971658]

Levy LS, Martin PA, Bidstrup PL, 1986 Investigation of the potential carcinogenicity of a range of chromium containing materials on rat lung. Br. J. Ind. Med 43, 243–256. 10.1136/oem.43.4.243. [PubMed: 3964573]

Li X, Poon C, Liu PS, 2001 Heavy metal concentration of urban soils and street dusts in Hong Kong. Appl. Geochem 16, 1361–1368. 10.1016/S0883-2927(01)00045-2.

Linton HR, 1972 inventor. Process for Making Silica-Coated Lead Chromate Pigments and Product Thereof Feb, 1. (United States Patent 3,639,133).

Lusby G, Hall C, Reiners J, 2015 Lead contamination of surface soils in Philadelphia from lead smelters and urbanization. Environ. Justice 8, 6–14. 10.1089/env.2014.0008.

Marques MRC, Loebenberg R, Almukainzi M, 2011 Simulated biological fluids with possible application in dissolution testing. Dissolut. Technol 18 (3), 15–28. 10.14227/DT180311P15.

Meza-Figueroa D, González-Grijalva B, Romero F, Ruiz J, Pedroza-Montero M, Rivero C.I. Del, Acosta-Elías M, Ochoa-Landin L, Navarro-Espinoza S, 2018 Source apportionment and environmental fate of lead chromates in atmospheric dust in arid environments. Sci. Total Environ 630, 1596–1607. 10.1016/j.scitotenv.2018.02.285. [PubMed: 29554776]

Murakami M, Nakajima F, Furumai H, Tomiyasu B, Owari M, 2007 Identification of particles containing chromium and lead in road dust and soakaway sediment by electron probe microanalyser. Chemosphere 67, 2000–2010. [PubMed: 17275880]

Naidoo S, Steyn WJ, 2018 Performance of themoplastic road-marking material. Journal of the South African Institution of Civil Engineers 60 (2). 10.17159/2309-8775/2018/v60n2a2.

O'Shea MJ, Vann DR, Hwang WT, Giere R, 2020 A mineralogic and chemical characterization of road dust in Philadelphia, PA. Environ. Sci. Pollut. Res 10.1007/s11356-019-06746-y.

Pacella A, Fantauzzi M, Turci F, Cremisini C, Montereali MR, Nardi E, Atzei D, Rossi A, Andreozzi GB, 2014 Dissolution reaction and surface iron speciation of UICC crocidolite in buffered solution at pH 7.4: a combined ICP-OES, XPS, and TEM investigation. Geochim. Cosmochim. Acta 127, 221–232.

Padoan E, Romè C, Ajmone-Marsan F, 2017 Bioaccessibility and size distribution of metals in road dust and roadside soils along a peri-urban transect. Sci. Total Environ 601–602, 89–98. 10.1016/j.scitotenv.2017.05.180.

Pier SM, Gallo MA, Umbreit TH, Connor TH, Gray D, Cappelleri FA, 1991 Silica encapsulation reduces bioavailability. Environ. Toxicol. Chem 10, 1247–1253. 10.1002/etc.5620101003.

Reeder RJ, Schoonen MAA, 2006 Metal speciation and its role in bioaccessibility and bioavailability. Reviews in Mineralogy & Geochemistry 64, 59–113.

Romieu I, Palazuelos E, Hernandez Avila M, Rios C, Munoz I, Jimenez C, Cahero G, 1994 Sources of lead exposure in Mexico City. Environ. Health Perspect 102, 384–389. 10.1289/ehp.94102384. [PubMed: 7523102]

Sidhu MK, Fernandez C, Khan MY, Kumar S, 1991 Induction of morphological transformation, achorage- dependent growth and pasminogen activators in nontumorigenic human osteosarcoma cells by lead chromate. Anticancer Res. 11, 1045–1053. [PubMed: 1888137]

Singh J, Pritchard DE, Carlisle DL, Mclean JA, Montaser A, Orenstein JM, Patierno SR, 1999 Internalization of carcinogenic lead chromate particles by cultured normal human lung epithelial cells: formation of intracellular lead-inclusion bodies and induction of apoptosis. Toxicol. Appl. Pharm 161, 240–248. 10.1006/taap.1999.8816.

Turner A, Lewis M, 2018 Lead and other heavy metals in soils impacted by exterior legacy paint in residential areas of south west England. Sci. Total Environ 619–620, 1206–1213. 10.1016/j.scitotenv.2017.11.041.

Turner A, Solman KR, 2016 Lead in exterior paints from the urban and suburban environs of. Sci. Total Environ 547, 132–136. 10.1016/j.scitotenv.2015.12.125. [PubMed: 26780138]

Turner A, Kearl ER, Solman KR, 2016. Lead and other toxic metals in playground paints from south West England. Sci. Total Environ 544, 460–466. 10.1016/j.scitotenv.2015.11.078. [PubMed: 26657391]

U.S. EPA, 2007 Estimation of Relative Bioavailability of Lead in Soil and Soil-Like Materials Using in vivo and in vitro Methods. 9285. Office of Solid Waste and Emergency Response, US EPA, Washington, pp. 7–77 OSWER.

United Nations, Department of Economic and Social Affairs, Population Division, 2014 World Urbanization Prospects: The 2014 Revision, Highlights (ST/ESA/SER.A/352).

United Nations, Environment Programme, the World Health Organization, 2019 ACTION PLAN for 2019–2020.The Global Alliance to Eliminate Lead Paint pp. 1–12.

Veblen DR, Wylie AG, 1993 Mineralogy of amphiboles and 1:1 layer silicates In: Guthrie GD Jr., Mossman BT (Eds.), Reviews in Mineralogy and Geochemistry. vol. 28 Mineralogical Society of America, Chantilly, VA, USA, pp. 61–137 (ISSN 0275–0279).

Vigliaturo R, Della Ventura G, Choi JK, Marengo A, Lucci F, O'Shea MJ, Perez-Rodriguez I, Giere R, 2018 Mineralogical charazterization and dissolution experiments in Gamble's solution of tremolitic amphibole from Passo di Caldenno (Sondrio, Italy). Minerals 8, 557 10.3390/min8120557. [PubMed: 31572620]

Wadanambi L, Dubey B, Townsend T, 2008 The leaching of lead from lead-based paint in landfill environments. J. Hazard. Mater 157, 194–200. 10.1016/j.jhazmat.2007.12.088. [PubMed: 18276069]

Walraven N, Bakker M, Van Os BJH, Klaver GT, Middelburg JJ, Davies GR, 2015 Factors controlling the oral bioaccessibility of anthropogenic Pb in polluted soils. Sci. Total Environ 506–507, 149–163. 10.1016/j.scitotenv.2014.10.118.

White K, Detherage T, Verellen M, Tully J, Krekeler MPS, 2014 An investigation of lead chromate (crocoite-PbCrO4) and other inorganic pigments in aged traffic paint samples from Hamilton, Ohio: implications for lead in the environment. Environ. Earth Sci 71, 3517–3528. 10.1007/s12665-013-2741-0.

Xu J, Wise PJ, Patierno SR, 1992 DNA damage induced by carcinogenic lead chromate particles in cultured mammalian cells. Mutat. Res 280, 129–136. [PubMed: 1378537]

Yoshinaga J, Yamasaki K, Yonemura A, Ishibashi Y, Kaido T, Mizuno K, Takagi M, Tanaka A, 2014 Lead and other elements in house dust of Japanese residences - source of lead and health risk due to metal exposure. Environ. Pollut 189, 223–228. 10.1016/j.envpol.2014.03.003. [PubMed: 24682073]

HIGHLIGHTS

- Simulated environmental and human interaction with yellow traffic paint ($PbCrO_4$).
- Some Pb and Cr were released into solution, especially into gut solution.
- Dimensional reductions observed after rainwater and Gamble's solution interactions.
- Silica coating encapsulating crocoite particles persisted during all interactions.
- Crocoite particles remained crystalline after all interactions.

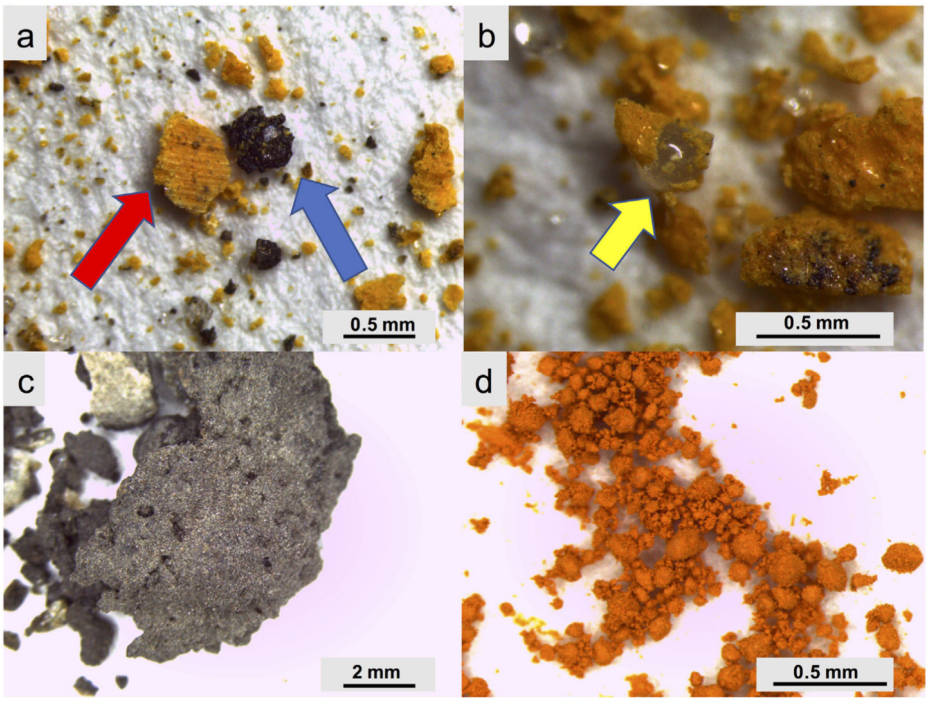

Fig. 1.

Optical microscopy pictures showing particles of YTP (a,b), asphalt (c), and standard $PbCrO_4$ (d). The red arrow points to a YTP particle, the blue to an asphalt particle, and the yellow to a glass bead. (For interpretation of the references to color in this figure caption, please view the web version of this article.)

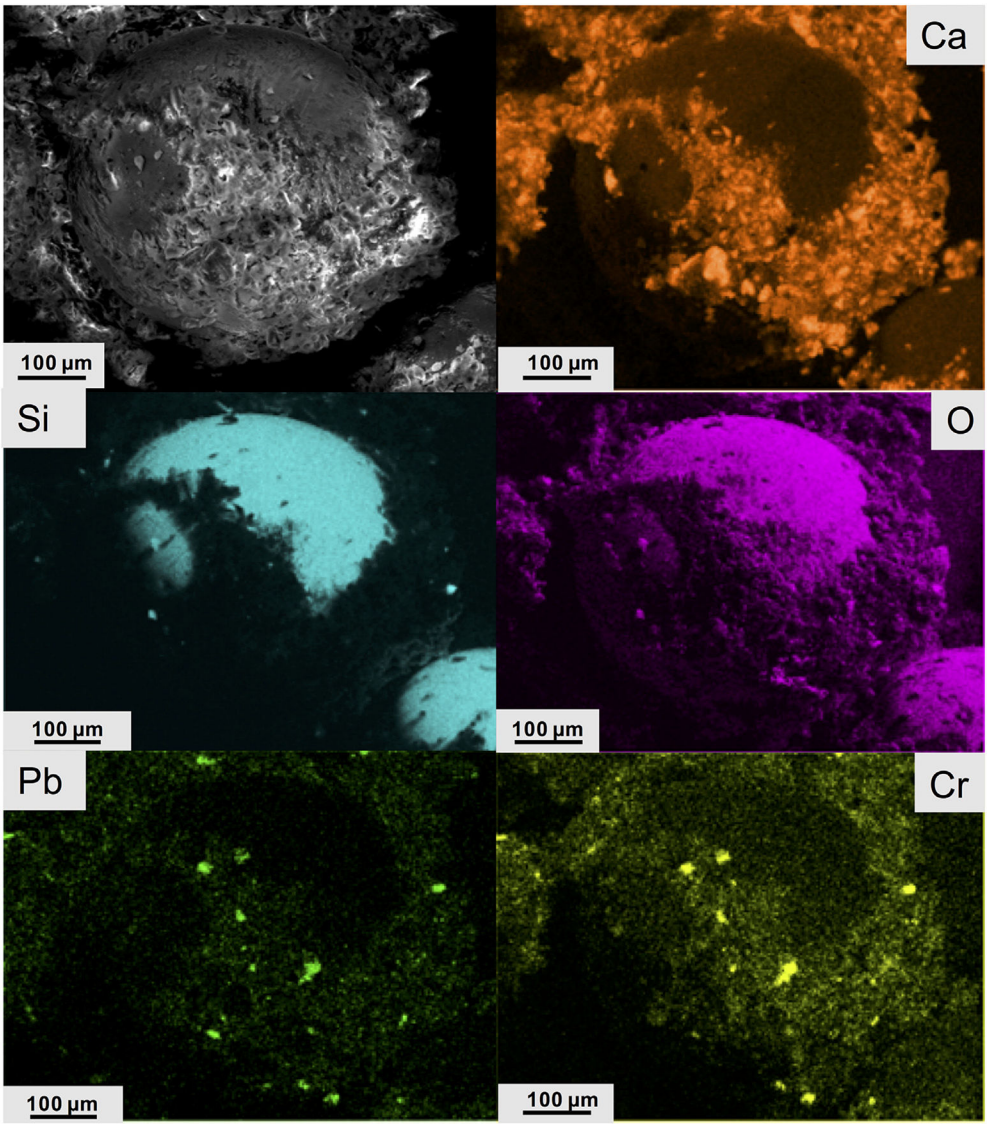

Fig. 2.

ESEM image (SE mode) showing a spherical object in YTP (top left); X-ray maps of the same area as that shown in the ESEM image displaying the distribution of Ca, Si, O, Pb, and Cr.

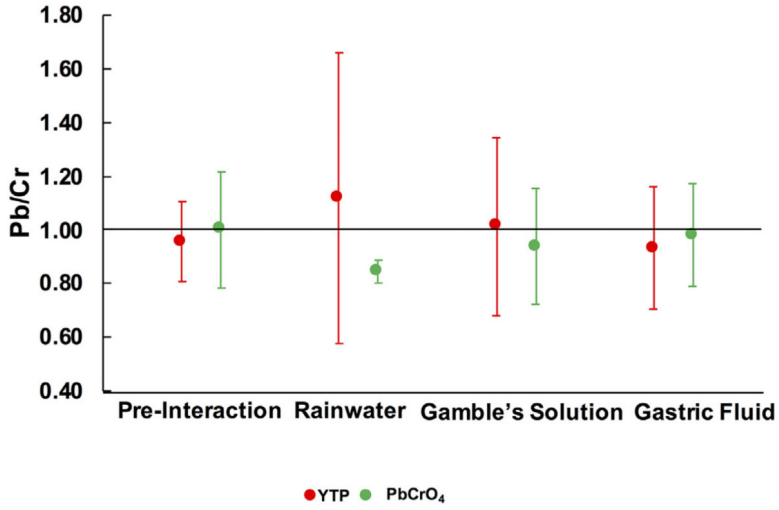

Fig. 3.

Values of Pb/Cr (at.%) in YTP particles and in standard $PbCrO_4$ before and after interaction with rainwater, Gamble's solution, and gastric fluid. These data were derived from ESEM-EDX analyses of 20 spots per sample. Error bars represent estimated total error.

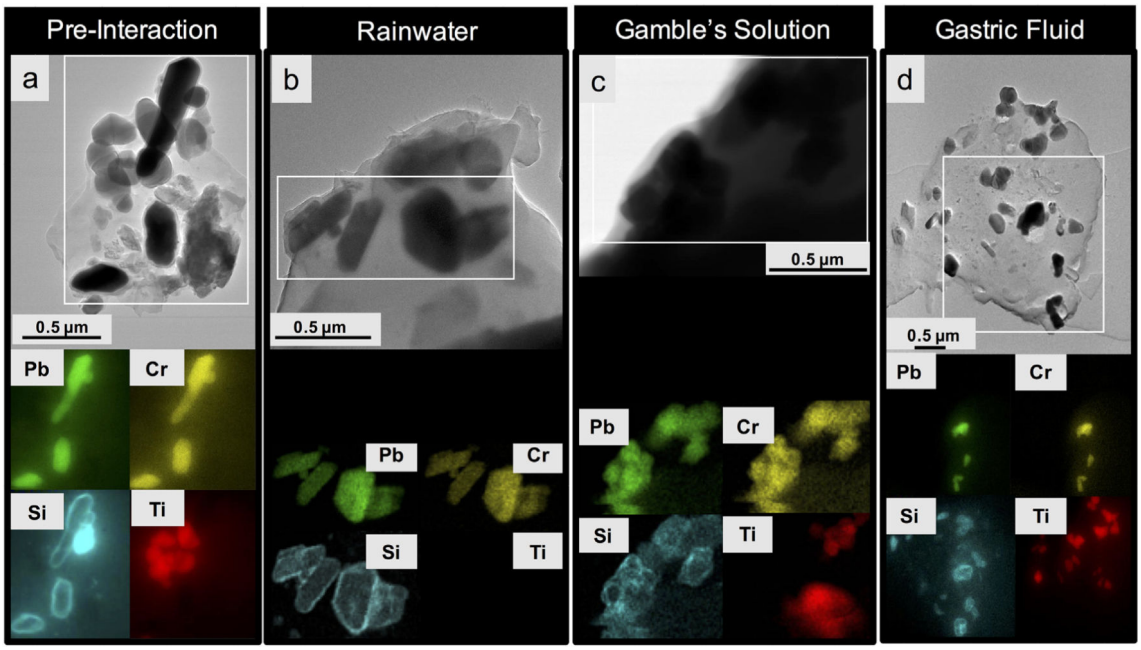

Fig. 4.

Bright-field TEM images (image d is in STEM mode) (top row) and associated STEM-EDX maps, showing the distribution of Pb, Cr, Si and Ti (bottom row) of YTP particles. Each map was collected from the rectangular area outlined in white in the TEM/STEM images shown in the top row; (a) particle before fluid exposure; (b) particle after rainwater interaction; (c) particle after exposure to Gamble's solution; (d) particle after gastric-fluid interaction. The images for b, c, and d were taken at the final experimental time points.

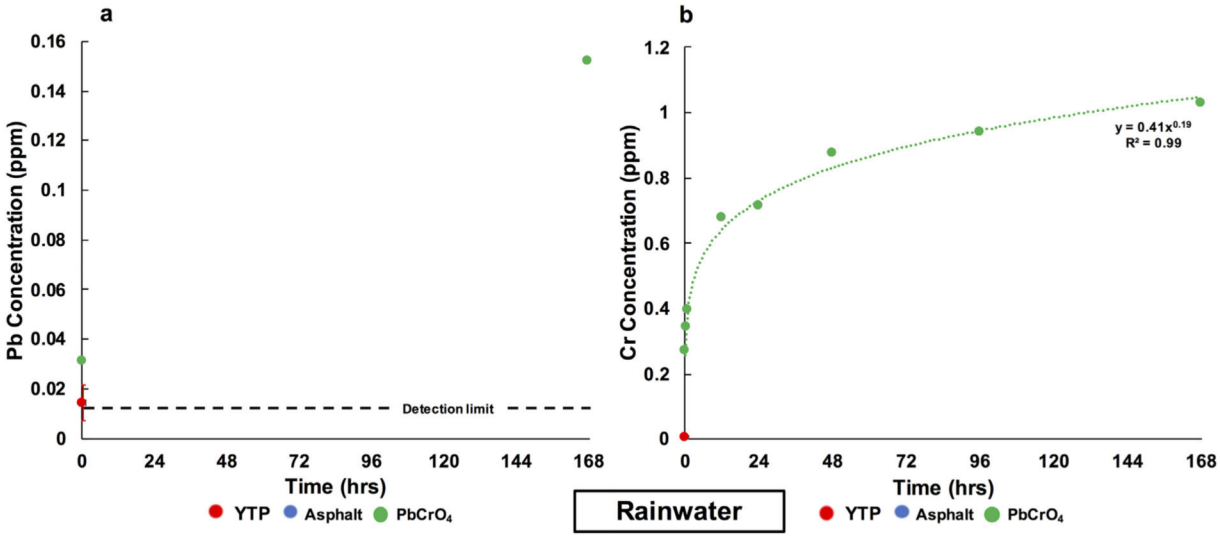

Fig. 5.

Evolution of the Pb (a) and Cr (b) concentrations in rainwater over 1 week. The red error bar represents the standard deviation (σ_{n-1}) of the data obtained from triplicate YTP experiments. Values below the detection limits (<0.013 ppm Pb and <0.003 ppm Cr) were not plotted. (For interpretation of the references to color in this figure caption, please view the web version of this article.)

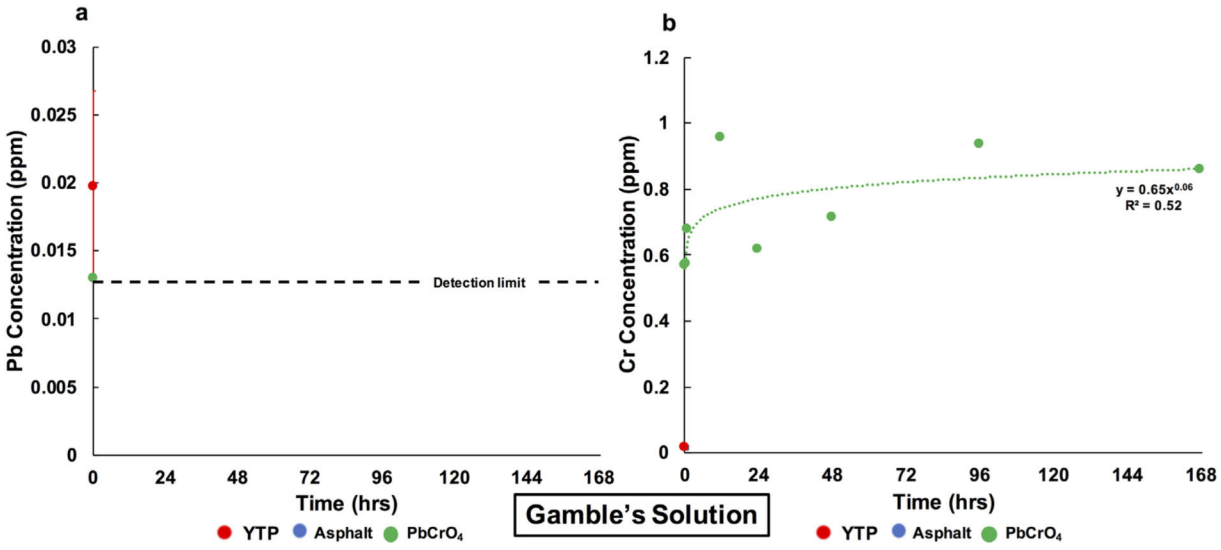

Fig. 6.

Evolution of the Pb (a) and Cr (b) concentrations in Gamble's solution over 1 week. The red error bar represents the standard deviation (σ_{n-1}) of the data obtained from triplicate YTP experiments. Values below the detection limits (<0.013 ppm Pb and <0.003 ppm Cr) were not plotted. (For interpretation of the references to color in this figure caption, please view the web version of this article.)

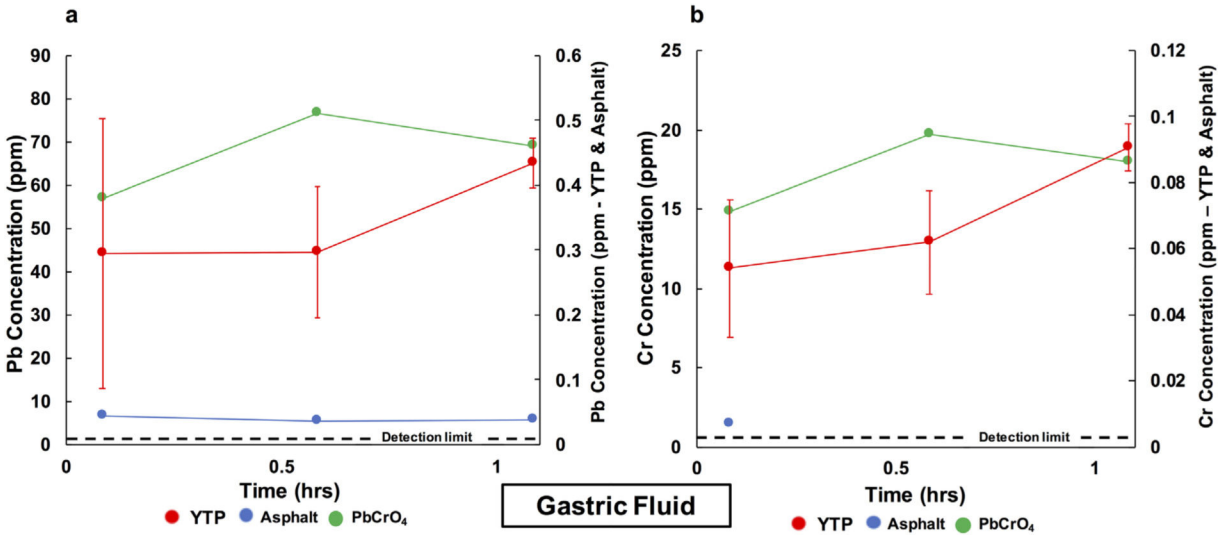

Fig. 7.

Evolution of the Pb (a) and Cr (b) concentrations in gastric fluid over 1 h. The red error bars represent the standard deviation (σ_{n-1}) of the data obtained from triplicate YTP experiments. Values below the detection limits (<0.013 ppm Pb and <0.003 ppm Cr) were not plotted. The detection limit relates to the secondary y-axis. (For interpretation of the references to color in this figure caption, please view the web version of this article.)

Table 1

Phases identified with PXRD and their estimated abundances in yellow traffic paint (YTP), asphalt, and standard $PbCrO_4$ samples (in wt%). The values for the YTP sample represent the average of three aliquots, with the standard deviation (σ_{n-1}) listed in parentheses.

Material	Calcite	Dolomite	Crocoite	Rutile	Quartz	Albite
Formula	$CaCO_3$	$CaMg(CO_3)_2$	$PbCrO_4$	TiO_2	SiO_2	$NaAlSi_3O_8$
YTP	70 (11)	14 (14)	5 (1)	4 (2)	1 (2)	–
Asphalt	–	23	–	–	7	70
$PbCrO_4$	–	–	100	–	–	–

Table 2

XRF concentrations of selected elements in YTP, asphalt, and standard $PbCrO_4$ (at.%).

Material	Pb	Cr	Ca	Si	Pb/Cr
YTP	0.90	0.75	41.08	4.70	1.20
Asphalt	<0.001	<0.001	27.00	15.32	–
$PbCrO_4$	24.51	19.96	0.54	<0.001	1.23

Table 3

Descriptive statistics and dimensional parameters for YTP particles before (pre-interaction) and after interaction with rainwater, Gamble's solution, and gastric fluid. The calculations are based on 100 particles per sample. D and d represent the major and minor axes of the particles, respectively. Morphology is the most common shape of the particle (Campbell, 1977; Veblen and Wylie, 1993). S and λ are dimensional parameters, V_e represents ellipsoidal volume, D_{ev} the equivalent-volume diameter, and S_A the surface area. Please refer to the methods section for details.

Fluid		D (μm)	d (μm)	Morphology (most frequent)	λ (unitless)	s (μm)	V_e (μm^3)	D_{ev} (μm)	S_A (μm^2)
Pre-Interaction	Mean	11.9	6.0	Equant	2.3	8.3	2173	8.3	1834
	σ_{n-1}	11.0	6.8		1.1	8.3	10,520	8.3	5076
	Max.	64.9	48.3		6.5	53.6	80,410	53.6	36,244
	Min.	1.5	0.7		1.0	1.0	0.5	1.0	14
Rainwater	Mean	6.7	3.3	Equant	2.1	4.6	170	4.6	469
	σ_{n-1}	6.1	2.6		0.9	3.6	384	3.6	746
	Max.	41.2	13.8		7.4	16.0	2130	16.0	4523
	Min.	0.5	0.3		1.0	0.4	0.1	0.4	3
Gamble's solution	Mean	7.3	3.7	Equant	1.9	5.1	287	5.1	618
	σ_{n-1}	6.9	3.0		0.6	4.4	767	4.4	1068
	Max.	35.5	15.2		4.2	23.3	6586	23.3	7454
	Min.	0.6	0.3		1.0	0.4	0.1	0.4	2
Gastric fluid	Mean	11.9	5.2	Equant	2.4	7.7	1942	7.7	1821
	σ_{n-1}	13.4	5.7		1.5	8.5	8487	8.5	4809
	Max.	73.3	36.3		12.0	51.6	71,872	51.6	35,654
	Min.	0.6	0.2		1.1	0.4	0.1	0.4	3

Table 4

Amounts of Pb and Cr extracted from original material (in %) at two time points (start and end of the experiments). Notes: $n = 3$ for YTP, with standard deviations in parentheses. "–" indicates that extracted concentrations were not detectable in the solutions.

		Pb (% extracted)		Cr (% extracted)	
Fluid	**Material**	**Start**	**End**	**Start**	**End**
Rainwater	YTP	0.03 (0.005)	–	0.05 (0.007)	–
Rainwater	$PbCrO_4$	0.01	0.02	0.20	0.75
Gamble's solution	YTP	0.04 (0.007)	–	0.18 (0.03)	–
Gamble's solution	$PbCrO_4$	<0.01	–	0.42	0.63
Gastric fluid	YTP	0.64 (0.010)	0.93 (0.145)	0.56 (0.078)	0.94 (0.131)
Gastric fluid	$PbCrO_4$	8.48	10.31	10.84	13.14